

# Determination of the penetration depth of ceramic blasting particles during composite peening

Michael Seitz<sup>a,\*</sup>, Wilfried V. Liebig<sup>a</sup>, Kay A. Weidenmann<sup>b</sup>

<sup>a</sup> Institute for Applied Materials (IAM-WK), Karlsruhe Institute of Technology (KIT), Engelbert-Arnold-Straße 4, 76131 Karlsruhe, Germany

<sup>b</sup> Institute of Materials Resource Management, Augsburg University, Universitätsstraße 1, 86159 Augsburg, Germany

## ARTICLE INFO

### Keywords:

Composite peening  
Solid particle erosion  
Impact  
Modelling penetration depth

## ABSTRACT

Composite peening is a process to embed ceramic particles into the surface of materials with the aim to improve the mechanical and tribological properties. These properties depend essentially on the penetration depth of the particles. In order to investigate the penetration depth achieved with composite peening, micrographs were taken and evaluated employing digital image processing.

In composite peening, the blasting particles penetrate the surface of the substrate depending on the process parameters. Models from the field of solid particle erosion were applied to predict the penetration depth of the particles. These analytical models can be used to evaluate the influence of specific process parameters on the penetration depth in composite peening. Furthermore, an additional model from ballistics was implemented. A good qualitative agreement was found between the analytical approaches and the experiments regarding the penetration depth after composite peening for the given system. In the future, this will allow estimating the penetration depth for other process parameters and materials for composite peening as well as for issues related to solid particle erosion.

## 1. Introduction

The penetration and embedding of particles into the surface of substrates is a phenomenon of many mechanical surface treatment processes [1]. Usually, the penetration of the blasting particles is not desired since foreign particles in the surface represent defects that reduce the service life of a component, especially in the case of fatigue or corrosion [2]. However, studies by Ando et al. [3] and Kameyama et al. [4] showed that embedding small ceramic blasting particles via micro peening could increase the component's surface hardness. The improved surface hardness may be promising in terms of high-temperature properties and tribological aspects.

The composite peening process was developed to increase the embedding of blasting particles based on micro peening. By adding a heating device, a process temperature close to the solidus temperature ( $T/T_S = 0.95$ ) increases the penetration depth of the ceramic blasting particles up to 30  $\mu\text{m}$  [5]. Furthermore, the authors identified the blasting pressure and the coverage to further influence the penetration depth. Furthermore, the properties of the blasting particles, such as density and shape, lead to different penetration depths.

Research in solid particle erosion is closely related to the

investigations of peening processes in mechanical surface treatment. Although the primary objective of erosion studies is to describe and reduce erosion, the experimental setup is similar to shot peening devices. However, it has been known for over 50 years that for ductile base materials, an initial increase in weight is due to the deposition and embedding of blasting particles [6,7]. Since then, several reviews have been published on the penetration and embedding of blasting particles and their fragments in solid particle erosion studies [8,9]. More recent contributions to this topic deal with the impact and penetration of single particles at high velocities and small particle sizes [10] or the numerical description of particle penetration [11].

The mechanical properties of the base material, in particular (yield) strength, Young's modulus and hardness, have been found to be a vital factor for the penetration of blasting particles. Most observations of embedded particle fragments have been made in ductile metals such as aluminum alloys and copper [6,7,12–24]. The process temperature also influences the indentation behavior by lowering the mechanical properties. Thus, blasting particles have also been detected in the surface of steels [25,26], tungsten [27] and titanium alloys [28] at elevated temperatures. Embedded particles in studies on polymers and composites have been reported by Refs. [7,29–33]. However, blasting particle

\* Corresponding author.

E-mail address: [Michael.Seitz@kit.edu](mailto:Michael.Seitz@kit.edu) (M. Seitz).

<https://doi.org/10.1016/j.wear.2022.204246>

Received 22 October 2021; Received in revised form 11 January 2022; Accepted 13 January 2022

Available online 29 January 2022

0043-1648/© 2022 The Authors.

Published by Elsevier B.V. This is an open access article under the CC BY-NC-ND license

(<http://creativecommons.org/licenses/by-nc-nd/4.0/>).

fragments could also be detected in metal-matrix composites and some ceramics as base material after erosion [34–37].

In addition to the mechanical properties of the base material, further parameter entail the embedding of particles and their fragments. The kinetic energy of the blasting particles also plays a decisive role. For example [38], could not detect any particles in the surface of EN AW-6061 during erosion tests using glass spheres (15  $\mu\text{m}$ ). The authors attributed this fact to the very low, but not further specified, velocity of the blasting particles. In a previous investigation, fragments of the glass spheres were observed in the base material of the same alloy (EN AW-6061) at a higher velocity of 93  $\text{ms}^{-1}$  [18].

Furthermore, the impact angle influences the vertical velocity of the blasting particles. In the case of a ductile base material, the number of embedded particles increases and the duration of the incubation phase is prolonged at larger impact angles [6,16,39]. The maximum of embedded particles can be observed at an impact angle of 90°.

The kinetic energy of the particle impact is influenced by the particle size and mass. Several studies are suggesting that below a threshold of about 20  $\mu\text{m}$ , no particle penetration can be observed at velocities in the range between 70  $\text{ms}^{-1}$  to 350  $\text{ms}^{-1}$  for several particle shapes and base materials [13,17,40–42]. This assumption is supported by studies with particles in this range [38,43]. However, it should be mentioned here that fragments of blasting particles smaller than 20  $\mu\text{m}$  have also been found in a Haynes Stellite surface at relatively low velocities of 20  $\text{ms}^{-1}$  to 50  $\text{ms}^{-1}$  [20,21].

Finally, some other factors affect the penetration depth of blasting particles in solid particle erosion. For example, while an increased mass flow rate leads to a shielding effect due to a higher amount of rebounding particles, the more particles penetrate, the higher the hardness ratio of particles to base material [44]. In addition, the penetration depends on the particle shape. The more angular the blasting particles, the more particles are embedded in the surface of the substrate [13,18,26]. An essential aspect of embedding angular particles is the particle orientation during impact [22,45].

It should be noted that the penetration of blasting particles depends on several factors that influence each other. The penetration depth increases with lower mechanical properties of the base material. Angular particles with high kinetic energy usually penetrate deeper into the base material. If these conditions are met, penetration depths in the higher micrometer range are observed in the literature, as shown in [Fig. 1].

## 2. Models for impact

Models describing the penetration depth of particles and the resulting wear are not only of interest in the context of solid particle erosion. Research in the field of ballistics is also addressing the calculation of the penetration depth of projectiles. A common aspect is a formulation based on the kinetic energy of the particles or projectiles and on the mechanical properties of the base material such as yield strength, Young's modulus or hardness. The particle or projectile shape also is an essential factor.

### 2.1. Model 1: Gotzmann, Beckmann

For solid particle erosion, various models exist for the analytical description of erosion rates [47]. The erosion models consider particle properties, base material properties and process parameters such as temperature, fluid dynamics and particle impacts.

There are also considerations for determining wear via the penetration depth of individual blasting particles. For example, Beckmann and Gotzmann assume plastic deformation for solid particle erosion of the base material as a requirement [48]. The penetration depth  $X_{GB}$

$$X_{GB} = R \left\{ \frac{2\rho_P}{3H_B} \left[ v_0^2 \sin^2 \alpha - \frac{4}{5} \frac{E'}{\rho_P \pi} \left( \frac{H_B}{E'} \right)^5 \right] \right\}^{1/2} \quad (1)$$

results as a function of the particle radius  $R$ , the hardness of the base material  $H_B$ , the reduced modulus of elasticity  $E'$ , the particle velocity  $v_0$ , the impact angle  $\alpha$  and the density of the particles  $\rho_P$ .

Here, the reduced modulus of elasticity

$$\frac{1}{E'} = \frac{1 - \nu_B^2}{E_B} + \frac{1 - \nu_P^2}{E_P} \quad (2)$$

depends on Young's modulus of the base material  $E_B$  and that of the blasting particle  $E_P$  and their Poisson ratios  $\nu_B$  and  $\nu_P$ , respectively [48].

Based on Eq. (1), the penetration depth, according to the model of Beckmann and Gotzmann, correlates with the particles' velocity and size. In contrast, the hardness of the base material is diametrical. In order to model the real conditions of solid particle erosion Eq. (1) can be extended by the corrective coefficient  $k = k_R k_\varphi$  [49]. With  $k_R$ , the shape of the blasting particles is being taken into account. The values range between 1 for almost spherical particles and increase up to a value of 2.7 for hard and angular particles. The second part of the corrective coefficient  $k_\varphi$  considers the particle flow. For a particle concentration of  $\varphi < 10 \text{ g/cm}^2\text{s}$ ,  $k_\varphi = 1$ . The higher the mass flow, the more likely is the rebounding particles' shielding effect, and consequently  $k_\varphi$  decreases. At a particle flow concentration of  $\varphi = 500 \text{ g/cm}^2\text{s}$ , the coefficient is still  $k_\varphi \approx 0.5$ .

### 2.2. Model 2: Ellermaa

A modification of the theory of Beckmann and Gotzmann is proposed by Ellermaa [50]. Due to the high velocity of the blasting particle, the use of the quasi-static hardness is insufficient according to Ellermaa. Instead, the use of the dynamic hardness  $H_D$  is proposed. The determination of the dynamic hardness can be obtained by dynamic indentation tests [51]. Approximately, the dynamic hardness  $H_D$  of fcc metals can be calculated by the equation

$$H_{D, fcc} = 1.7 HB \quad (3)$$

with the Brinell hardness  $HB$  [50]. For bcc and hex crystal lattices, Ellermaa summarizes the relationship between dynamic and static hardness with the equations

$$H_{D, bcc} = 1.3 \text{ GPa} + 1.8 HB \quad (4)$$

and

$$H_{D, hex} = 0.58 \text{ GPa} + 1.8 HB. \quad (5)$$

Kleis and Kagnur explain the influence of the crystal lattice by the different number of slip systems [51].

The following equation based on experimental results calculates the penetration depth  $X_E$ :

$$X_E = R \left[ \frac{2\rho_P}{3H_D} (v_0^2 \sin^2 \alpha) \right]^{1/2} \quad (6)$$

Adding the influence of the particle size  $k_d$  and the hardness ratio between particle and base material  $k_H$  to the corrective coefficient is also discussed. Below the limit of a mean diameter  $d$  of 120  $\mu\text{m}$ , the corrective coefficient decreases with particle size:  $k_d = d/120$ . The hardness corrective coefficient only applies when the hardness of the base material is similar to the hardness of the blasting particles. Above  $H_P/H_B > 1.6$ , the corrective coefficient is  $k_H = 1$ .

### 2.3. Model 3: Chen, Li

Based on the first analytical models from 1945 [52] describing penetration mechanisms by quasi-static equations, analytical and experimental methods have evolved in ballistics to predict penetration behavior [53]. In these models, a dynamic cavity expansion equation describes the material behavior at the impact of the projectile at high

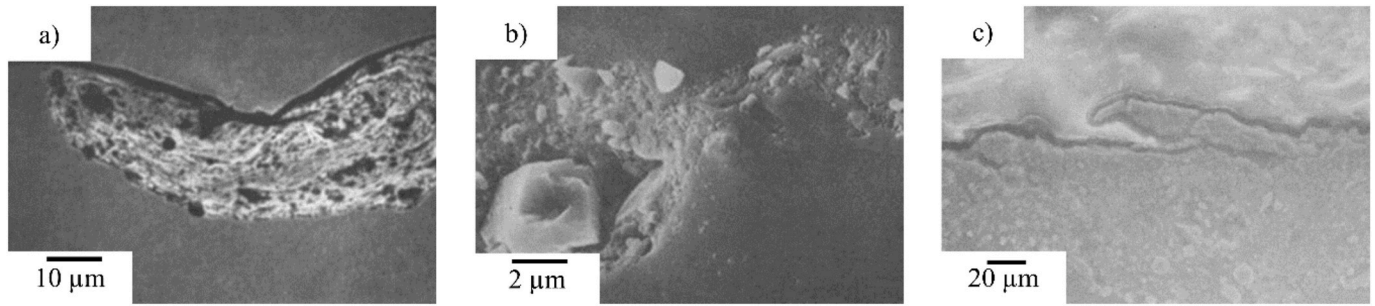


**Fig. 1.** Micrographs of embedded blasting particles for various base materials. a) Copper at room temperature with glass spheres (70  $\mu\text{m}$ ) [15]. b) Copper at room temperature with  $\text{Al}_2\text{O}_3$  particles (35  $\mu\text{m}$ –65  $\mu\text{m}$ ) [12].<sup>2</sup> c) Aluminum (EN AW-1100) at room temperature with SiC particles (600  $\mu\text{m}$ ) [46].<sup>3</sup>

velocities [54–56]. The Best number  $BN = \rho_B v^2 / R_p$  can be used as a characteristic value for the transition of elastic, elastic-plastic and hydrodynamic deformation behavior [57–59].  $\rho_B$  is the density and  $R_{eS,B}$  is the yield strength of the base material. Some formulations use the hardness of the base material instead of the yield strength [53,60]. The particle velocity  $v$  contributes quadratically to the equation. For a Best number  $BN < 10^{-3}$ , a purely elastic behavior can be assumed. The base material begins to deform plastically for a Best number  $BN > 10^{-3}$  [58, 59]. Above a Best number higher than  $BN \approx 100^1$  it can be assumed that the base material behaves like a fluid, and hydrodynamic deformation mechanisms describe the impact and subsequent deformation of the base material [60].

The final penetration depth  $X_{CL}$  of the projectile calculated by Chen and Li [61] is then given by

$$X_{CL} = \frac{2m}{\pi d_p^2 B \rho_B N_2} \ln \left( 1 + \frac{B \rho_B v_0^2 N_2}{A R_{eS,B} N_1} \right). \quad (7)$$

The material parameters of the base material  $R_{eS,B}$  as yield strength and  $\rho_B$  as density are used in the equation. The influence of the projectile shape is represented by the two dimensionless projectile shape factors  $N_1$  and  $N_2$ .  $m$  and  $d_p$  are the mass and the diameter of the projectile, respectively.

The relationship between the dimensionless projectile shape factors  $N_1$  and  $N_2$  and friction complicates the calculation for dynamic processes. Experimentally determined values of shape factors of different projectile geometries at the impact on EN AW-6061 are summarized by Chen and Li in [Table 1] [61].

The material constant  $A$  can be determined for an ideal elastic-plastic

**Table 1**  
Shape factors for different projectile geometries.

	$N_1$	$N_2$
Spherical shape	1.16	0.54
Ogive shape	1.09	0.11
Conical shape	1.30	0.13

<sup>1</sup> Sundararajan and Shewmon [60] calculate the Best number via the hardness of the base material. The Best number given here applies to the yield strength of the base material.

<sup>2</sup> Reprinted, with permission, from L.K. Ives, A.W. Ruff, *Electron Microscopy Study of Erosion Damage in Copper*, in: W.F. Adler (Ed.), *Erosion: prevention and useful applications*, ASTM International, Philadelphia, 1979, 5-35., copyright ASTM International, 100 Barr Harbor Drive, West Conshohocken, PA 19428.

<sup>3</sup> Reprinted, with permission, from I. Finnie, A. Levy, D.H. McFadden, *Fundamental Mechanisms of the Erosive Wear of Ductile Metals by Solid Particles*, in: W.F. Adler (Ed.), *Erosion: prevention and useful applications*, ASTM International, Philadelphia, 1979, pp. 36–58., copyright ASTM International, 100 Barr Harbor Drive, West Conshohocken, PA 19428.

material by the quasi-static expansion of a spherical cavity by using Young's modulus  $E$ , the yield strength  $R_{eS,B}$  and the Poisson's ratio  $\nu_B$  [54].

$$A = \frac{2}{3} \left\{ 1 + \ln \left[ \frac{E}{3(1-\nu_G)R_{eS,G}} \right] \right\} \quad (8)$$

In contrast to parameter  $A$ , the second material constant  $B$  for aluminum ranges between  $B = 0.983$  [62,63] and  $B = 1.133$  [64].

All of the analytical approaches of the penetration depth are summarised and shown in [Fig. 2] over a temperature range between 0.32  $T/T_S$  (room temperature) and slightly below the melting point of EN AW-1050. Due to the temperature-related decrease in the mechanical properties, the blasting particles penetrate deeper into the base material. The use of particles with a higher diameter, density and velocity also increases the penetration depth. The shape of the particles is also included in the calculation of the penetration depth via shape factors. The more angular the particles, the higher the penetration depth. The models of Beckmann and Gotzmann or Ellermaa differ only slightly in their calculated penetration depth due to the same basic physical principle describing the penetration of the particles. However, there are slight differences in the penetration depth due to the use of the static

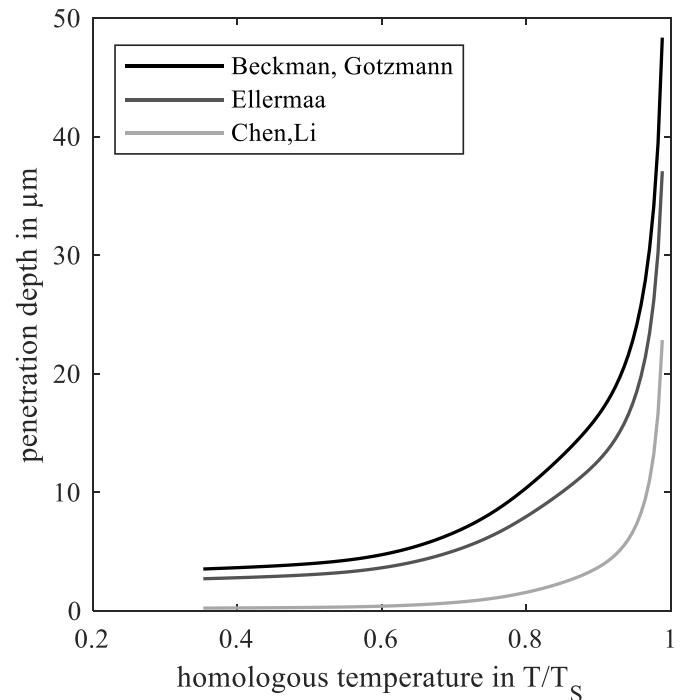


**Fig. 2.** Comparison between different models for calculating the penetration depth for the system  $\text{Al}_2\text{O}_3$  (grain size F600) and EN AW-6082 with a blasting pressure of 7 bar.

hardness values in the case of Beckmann and Gotzmann in contrast to the dynamic hardness in the case of Ellermaa. As used by Chen and Li, the use of hydrodynamic assumptions leads to significantly lower penetration depths.

### 3. Experimental section

#### 3.1. Materials

Two different aluminum alloys were selected as base material for composite peening. The technically pure alloy EN AW-1050 and the wrought alloy EN AW-6082. The sheet material was purchased from BIKAR-METALLE (Bad Berleburg–Raumland, Germany). The chemical composition of both alloys is shown in [Table 2] and is in accordance with the DIN EN 573 standard [65].

Since the process of composite peening takes place at temperatures above 400 °C, the high-temperature characteristics of the aluminum alloys are of interest. [Fig. 3]. gives an overview of the yield strength and the Young's modulus of the two aluminum alloys EN AW-1050 and EN AW-6082 at elevated temperatures. The mechanical properties shown were determined by tensile tests by using the DIL805 A/D dilatometer from Bähr Thermoanalyse GmbH (Hüllhorst, Germany).

By increasing the temperature, both the yield strength and the Young's modulus successively decrease. Thus, the mechanical properties of technically pure aluminum are lower than those of the alloy EN AW-6082 in general. Up to a temperature of 370 °C, literature values confirm the determined Young's modulus in the case of an aluminum-magnesium-silicon alloy (EN AW-6061) [66]. The process temperatures for composite peening are presented as homologous temperatures in this work. For the sake of completeness, the mechanical properties of yield strength and Young's modulus for both alloys are presented versus the homologous temperature in [Fig. 4].

The models by Gotzmann and Beckmann, or Ellermaa, utilize the (dynamic) hardness instead of the yield strength to represent the mechanical properties. To present the hardness as a function of temperature, a linear relationship with the yield strength taken from the dilatometer analysis was chosen [67,68]. [Fig. 5]. gives an overview of the hardness as a function of the homologous temperature of the alloys EN AW-1050 and EN AW-6082.

Three different ceramics were selected as blasting particles: aluminum oxide ( $\text{Al}_2\text{O}_3$ ), silicon carbide (SiC) and tungsten carbide (WC).  $\text{Al}_2\text{O}_3$  and SiC were purchased from Arteka e.K. (Backnang - Waldrems), WC from H.C. Starck GmbH (Goslar). [Fig. 6]. shows scanning electron micrographs of the three different ceramic particles with grain size F600, corresponding to a weight-average particle size of 9.3  $\mu\text{m}$  [69]. While  $\text{Al}_2\text{O}_3$  and SiC have an angular shape, the WC particles are spherical.

Additionally,  $\text{Al}_2\text{O}_3$  with grain size F320 was used as blasting particle, which according to the standard, results in a weight-averaged particle size of 29  $\mu\text{m}$ . Particle size measurements by laser diffraction are given in [Table 3].  $D_{s10}$  and  $D_{s90}$  values provide information on the particle size distribution. While 10% of the particles are smaller than the  $D_{s10}$  value, the diameter of 10% of the particles is larger than the  $D_{s90}$  value. Slight variations of the particle size distribution are possible over different batches. The average particle size in F600 grain size ranged between 8  $\mu\text{m}$  and 13  $\mu\text{m}$  for  $\text{Al}_2\text{O}_3$ .

The density of the blasting particle material  $\rho_p$  listed in [Table 4] are given in the material database of CES EduPack [70]. Beckmann and Gotzmann suggest a particle shape factor  $k_R$  of 1.6–1.9 for angular  $\text{Al}_2\text{O}_3$

**Table 2**  
Chemical composition of both aluminum alloys.

Wt%	Al	Mg	Si	Fe	Cu	Mn
EN AW-1050	99.52	<0.01	0.10	0.30	<0.01	<0.01
EN AW-6082	Base	0.90	0.88	0.40	0.08	0.43

particles (corundum) based on studies by Tadolder. For analytical modelling of the penetration depth, a value of  $k_R = 1.6$  is used in this work. No explicit value of the particle shape factor is given for SiC. As a substitute, the proposed shape factor for an edged glass of  $k_R = 1.9$  is used. For roughly spherical particles, such as the WC particles used in this work, a particle shape factor of  $k_R \approx 1$  can be assumed [49].

#### 3.2. Composite peening

A schematic setup of the composite peening system is depicted in [Fig. 7]. A heating device (heating plate, Typ L3/11, Nabertherm GbmH, Lilienthal) was added to the AccuFlo microblasting system from Comco Inc. (Burbank, USA) and the CNC machine, including a control unit from isel Germany AG (Eichenzell). Due to the temperature-related reduction of the mechanical parameters, initial studies showed an increase in the penetration depth of the ceramic blasting particles at enhanced process temperatures [71].

The selected peening parameters are shown in [Table 5]. In preliminary tests, lower temperatures were additionally chosen for the aluminum alloy EN AW-1050 to cover a wider temperature range. Compressed air at room temperature cause cooling of the specimen surface due to the peening process. The cooling could be limited to a maximum of 120 K by the selected process parameters. The temperature gradient was taken into account in that each blasting path was run symmetrically (in positive and negative x-direction). The temperature at the beginning of the blasting process was used as the reference.

In addition to the process temperature, the blasting pressure and the coverage have been varied. Constant parameters were the speed, working distance, nozzle diameter, impact angle and path distance.

#### 3.3. Resulting system parameters

The influence of the blasting pressure on the velocity of the blasting particles was published by Weingärnter et al. for the AccuFlo microblasting system, depicted in [Fig. 8] [72]. For a pressure of 1 bar, the abrasive velocity is below 100  $\text{ms}^{-1}$ . Increasing the pressure leads to velocities just below 200  $\text{ms}^{-1}$  at 7 bar. Measurements of velocity using laser shadowgraphy led to slightly lower velocities for the same blasting system by Getu et al. [31]. However, in this case, larger beam particles were used, and particle size was found to be anticorrelated with particle velocity. Kikuchi et al. also found a slower particle velocity for larger blasting particles [73].

Depending on the blasting pressure (4 bar or 7 bar), particle velocities of 171  $\text{ms}^{-1}$  to 193  $\text{ms}^{-1}$  and a blasting path width of 1.28 mm–1.81 mm were obtained. In combination with a path distance of 1 mm, this resulted in an overlap of 28%–81%. The deflection of the Almen strips varied in a range of 0.033 mmN and 0.047 mmN. The mass flow rate was 8.2  $\text{g min}^{-1}$  to 14.8  $\text{g min}^{-1}$  depending on the blasting pressure. With the process parameters described above, more than one million particles impact the surface per square millimeter. This results in multiple impingements of the blasting particles on the same spot.

#### 3.4. Microstructural characterization

To determine the penetration depth, images were taken on micrographs by using the VHX-600DSO digital microscope from KEYENCE Corporation (Osaka, Japan). For each process parameter, the penetration depth of three experiments were evaluated and the standard deviation was indicated with scatter bars. A detailed description of the preparation routine for the micrographs is already given by the authors in a previous publication [74]. The penetration depth was evaluated with digital image processing (DIP). For this purpose, the recorded individual images were stitched by using ImageJ. The evaluated length was 10 mm per micrograph. Subsequently, an evaluation routine in Matlab was used to determine the penetration depth for each pixel in the horizontal direction. The image resolution for this analysis was 0.38  $\mu\text{m}$ .

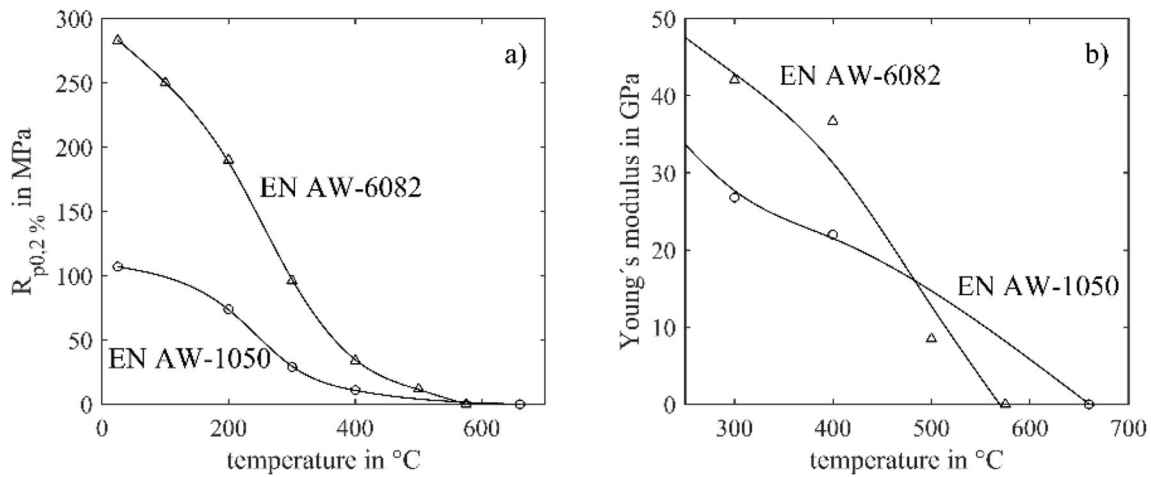


Fig. 3. a) High-temperature properties of yield strength and b) Young's modulus of EN AW-1050 and EN AW-6082.

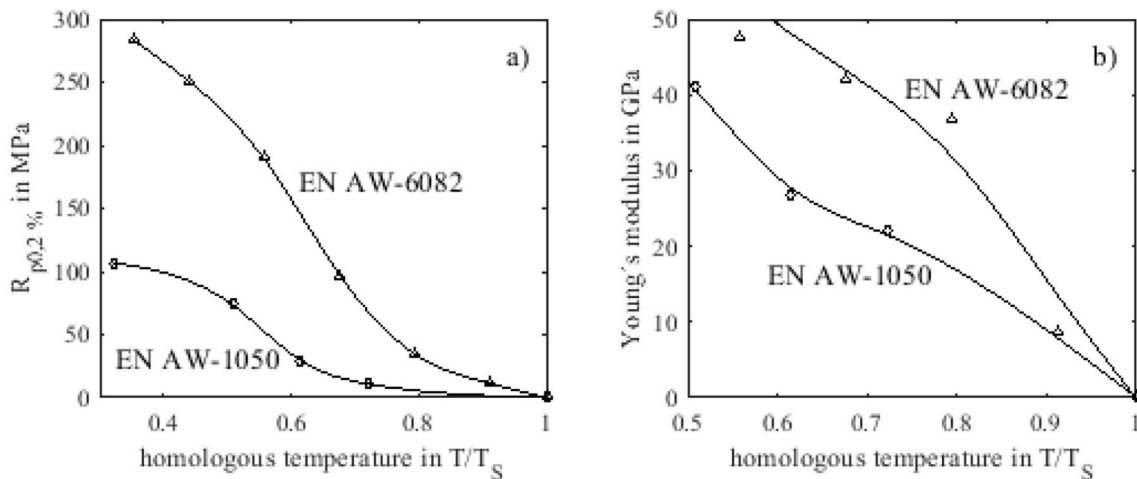


Fig. 4. a) High-temperature properties of yield strength and b) Young's modulus of EN AW-1050 and EN AW-6082 from [Fig. 3] in homologous temperature scale.

The relationship between volume content of the ceramic particles and the distance to the specimen surface of the alloy EN AW-1050 is shown in [Fig. 9]. For all investigated parameters, a similar trend of the ceramic fraction is visible.

Oxide fragments almost completely cover the surface. The proportion of ceramic phase decreases linearly with increasing distance from the specimen surface. Isolated fragments penetrate slightly deeper, which explains the flattening of the curve at greater surface distances. The surface distance for a reinforcement fraction of 1% is shown in the following section for different process parameters.

## 4. Results

### 4.1. Micrographs

The micrographs of the EN AW-6082 alloy after composite peening in [Fig. 10] show a hill-valley structure, described in detail elsewhere [75]. It can be seen that the blasting particle accumulations are primarily found in the valleys. These particle accumulations range a few micrometers from the specimen surface to the interior. In contrast, only very small amounts of ceramic particles are found on the hills. The same features are observable for the aluminum alloy EN AW-1050 [76].

[Fig. 10a] shows an image with  $Al_2O_3$  particles. The accumulations of the particle fragments can be seen as dark areas at irregular intervals. The white dots inside the material represent precipitates of the

aluminum alloy. When SiC is used as blasting particles, the surface is less humpy, as can be seen in [Fig. 10b]. Likewise, almost no particle fragments are visible on the surface. The good visibility of the WC particles is due to the large density difference between WC and the aluminum base material [Fig. 10c]. The hill-valley structure and roughness, as well as the penetration depth, are greatest for this material combination. The ceramic particles are visible on the surface over the entire width of the image.

### 4.2. Influence of the process temperature

Due to the temperature dependence of the mechanical properties, the process temperature is of vital importance for the penetration depth of the blasting particles in composite peening. [Fig. 11]. shows this relationship using  $Al_2O_3$  particles (grain size F600) as blasting particles and the aluminum alloy EN AW-1050 as base material at an blasting pressure of 7 bar. In addition, the results from preliminary tests at lower process temperatures for a fourfold coverage are shown.

The preliminary tests' penetration depth evaluated in the micrographs reveals negligible temperature dependence up to a homologous temperature of 0.6  $T/T_S$ . A higher process temperature results successively in an increase of the penetration depth. The model of Beckmann and Gotzmann also reproduces this behavior. The dashed lines indicate the particle size distribution range in the following figures with the penetration depths for larger particles (Ds90) and smaller particles

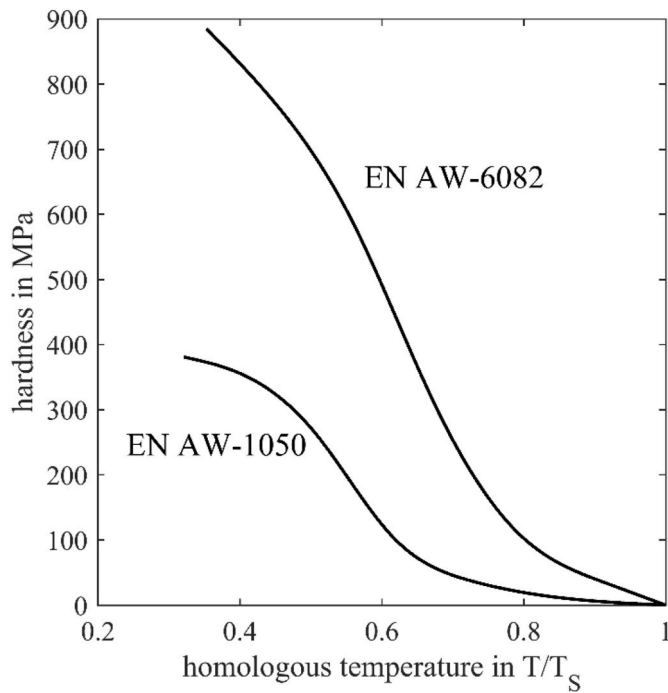


Fig. 5. Temperature dependence of the hardness of EN AW-1050 and EN AW-6082.

(Ds10) of grain size F600. The penetration depth calculated by the model increases above a process temperature of 0.5  $T/T_S$ . This is due to a softening of the base material in this temperature range, as shown in [Fig. 5]. The penetration depth evaluated in the micrographs and the

model agree qualitatively to a process temperature of 0.8  $T/T_S$ . Higher process temperatures do not yield a pronounced increase in penetration depth, and the model of Beckmann and Gotzmann overestimates the measured penetration depth. In the case of twofold coverage, a lower penetration depth is measured. The maximum penetration depth of 33.8  $\mu\text{m}$  is observed using a fourfold coverage with 7 bar and a 0.9  $T/T_S$  process temperature.

4.3. Influence of the base material

A lower penetration depth is observed for the EN AW-6082 alloy as base material, as shown in [Fig. 12]. The higher mechanical properties even at high process temperatures leads to penetration depths of 13.5  $\mu\text{m}$ , which is significantly less compared to EN AW-1050. Due to the

Table 3

Weight-averaged particle size of the blasting particles (Karlsruhe Institut of Technology, IAM-ESS).

	$\text{Al}_2\text{O}_3$		SiC	WC
	F320	F600	F600	F600
	Mm	$\mu\text{m}$	$\mu\text{m}$	$\mu\text{m}$
Ds10	25.3	8.3	5.3	9.0
Ds50	36.4	13.2	9.6	15.6
Ds90	53.0	19.8	15.5	26.1

Table 4

Particle shape factor and density of the blasting particles.

	$\text{Al}_2\text{O}_3$	SiC	WC	Literature
$K_R$	1.6	1.9	1.0	[48,49]
$\rho_P$	3990 $\text{kgm}^{-3}$	3100 $\text{kgm}^{-3}$	15,700 $\text{kgm}^{-3}$	[70]

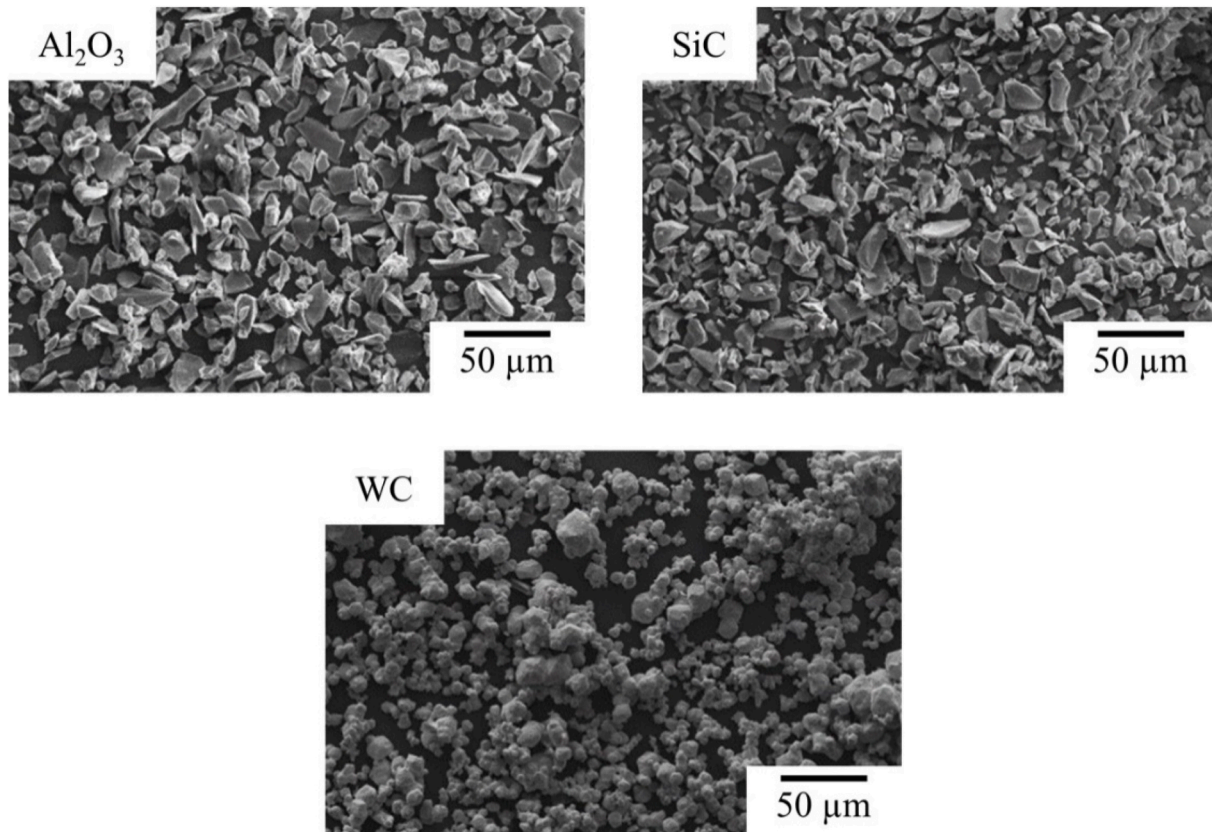


Fig. 6. Scanning electron images of the used blasting particles: aluminum oxide ( $\text{Al}_2\text{O}_3$ ), silicon carbide (SiC) and tungsten carbide (WC).

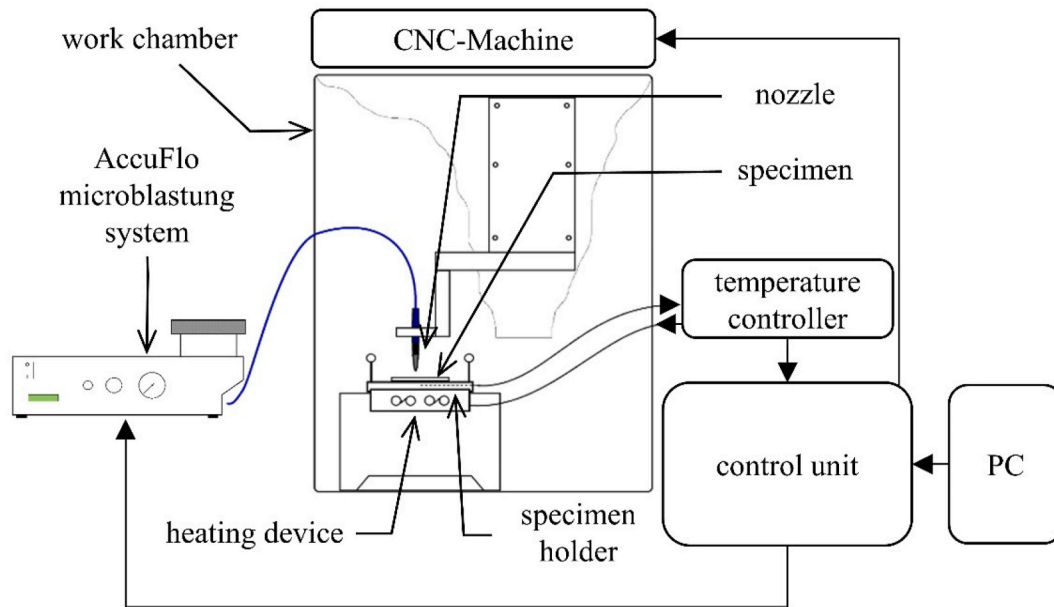


Fig. 7. Schematic setup of the composite peening system [5].

Table 5  
Overview of the composite peening parameters.

Homologous temperature	$T/T_S$	-	0.8; 0.9; 0.95
Blasting pressure	$p$	bar	4; 7
Coverage	$z$	-	2; 4
Feed rate	$v_F$	$\text{mms}^{-1}$	8
Working distance	$a$	mm	10
Nozzle diameter	$d_d$	mm	0.76
Impact angle	$\alpha$	$^\circ$	90
Path distance	$b$	mm	1

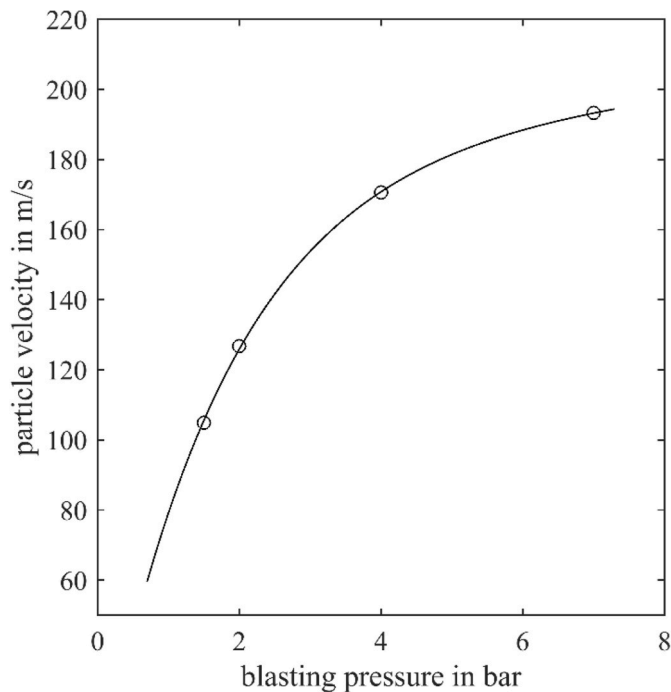


Fig. 8. Influence of the blasting pressure on the velocity of the blasting particles for the AccuFlo microblasting system (given by Comco Inc.) according to Ref. [72].

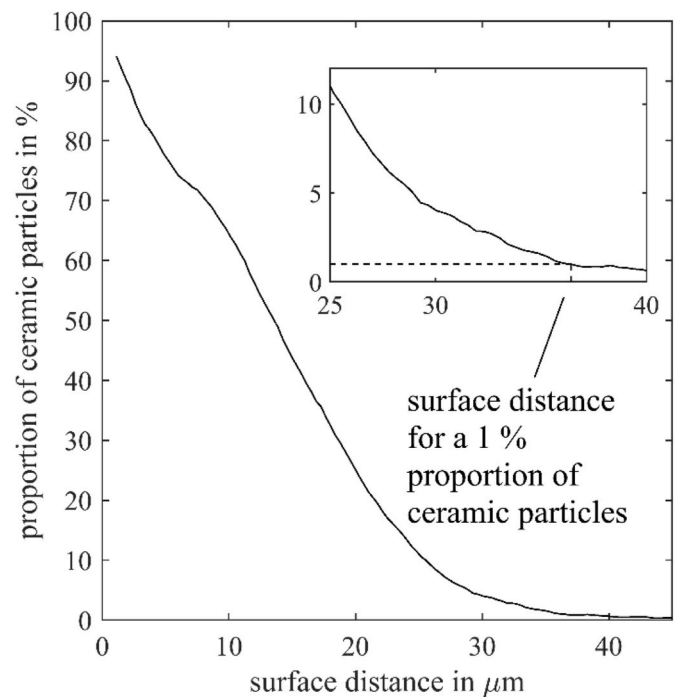


Fig. 9. Proportion of ceramic particles depending on the distance to the surface. EN AW-1050 with  $\text{Al}_2\text{O}_3$  particles ( $T/T_S = 0.9$ ,  $z = 4$ ,  $p = 7$  bar).

higher hardness of the base material, the model of Beckmann and Gotzmann also results in a lower penetration depth. For homologous temperatures up to  $0.9 T/T_S$ , the results of the penetration depth from the micrographs are in the scatter range of the particle size distribution. In the higher homologous temperature of  $0.95 T/T_S$ , the model also overestimates the penetration depth.

#### 4.4. Influence of the blasting pressure

The velocity of the particles depends on the blasting pressure, as shown in [Fig. 8]. The increase in velocity due to a change in pressure

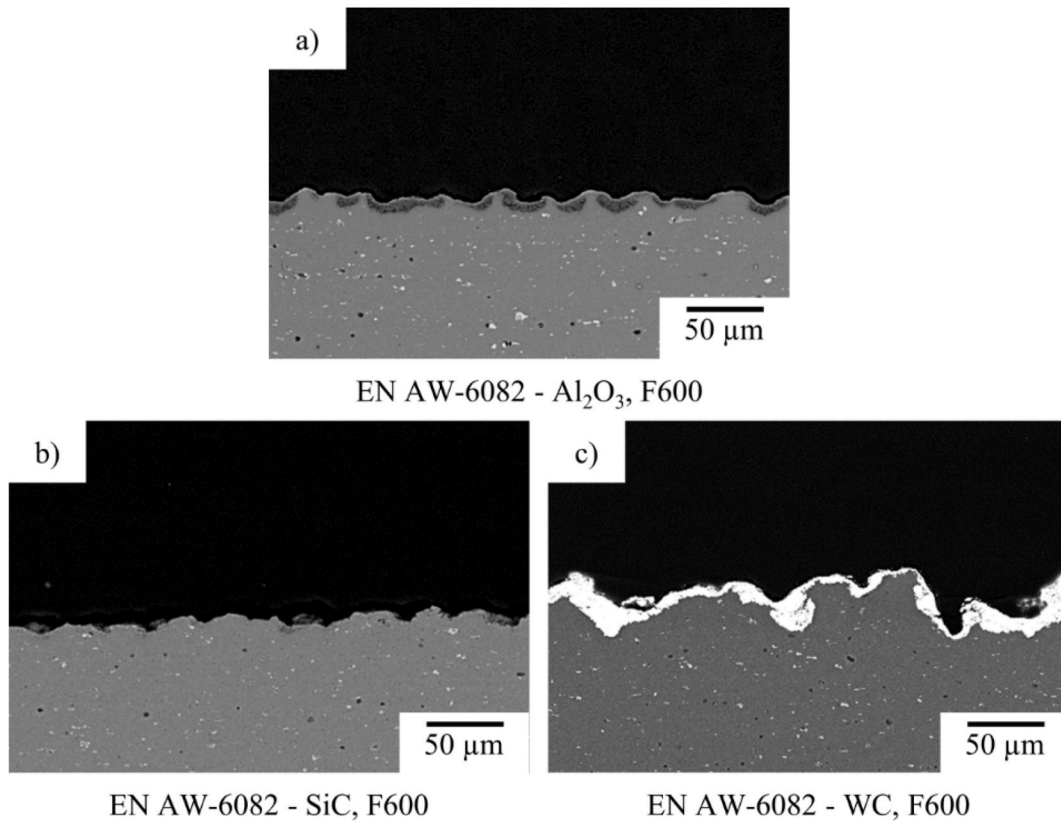


Fig. 10. Micrographs of the composite peened surfaces of EN AW-6082 with a) Al<sub>2</sub>O<sub>3</sub> b) SiC and c) WC.

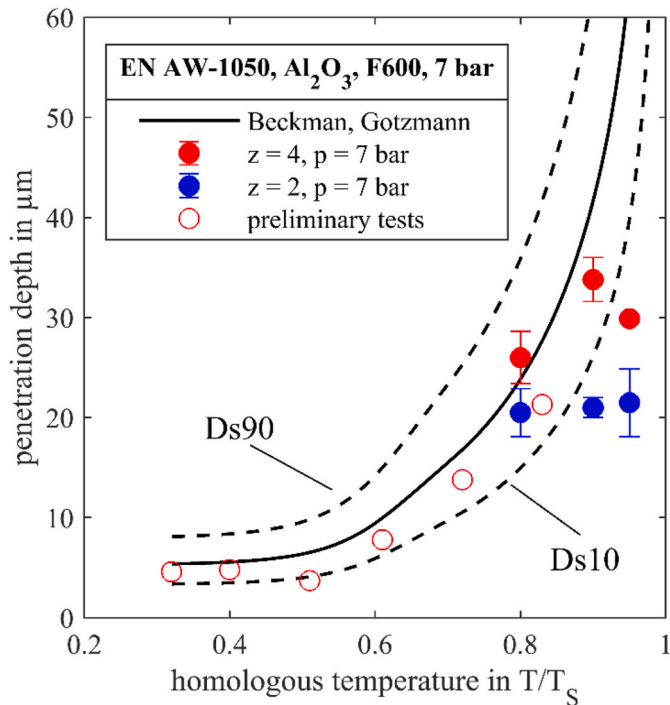


Fig. 11. Comparison of the penetration depth from preliminary tests (maximum penetration depth) and (particle fraction of 1% according to [Fig. 9]) of the Al<sub>2</sub>O<sub>3</sub> particles for the base material EN AW-1050 at an blasting pressure of 7 bar with the model of Beckmann and Gotzmann.

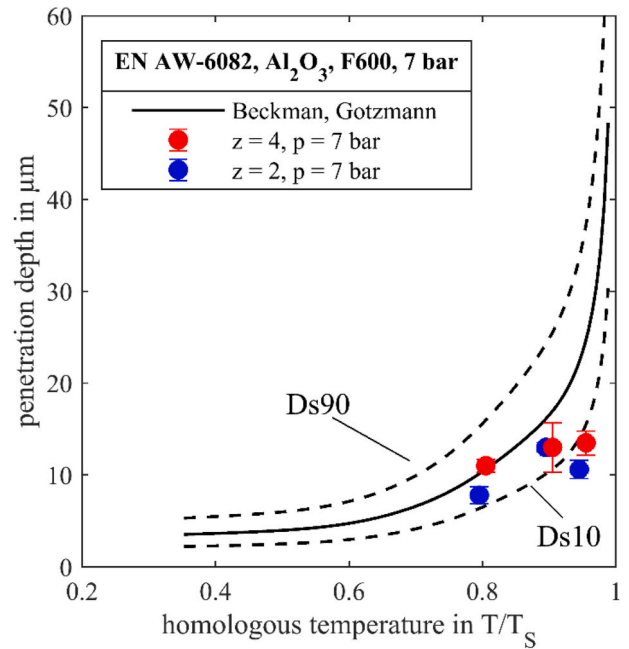


Fig. 12. Comparison of the penetration depth of Al<sub>2</sub>O<sub>3</sub> particles for the alloy EN AW-6082 for an blasting pressure of 7 bar with the model of Beckmann and Gotzmann.

from 4 bar to 7 bar is only 13% (171 ms<sup>-1</sup> to 193 ms<sup>-1</sup>) for the AccuFlo microblasting system. Since the penetration depth calculated by the model of Beckmann and Gotzmann is linearly dependent on the velocity, a pressure of 4 bar shows only a minimal change in the penetration depth in [Fig. 13] compared to a pressure of 7 bar in [Fig. 8]. The

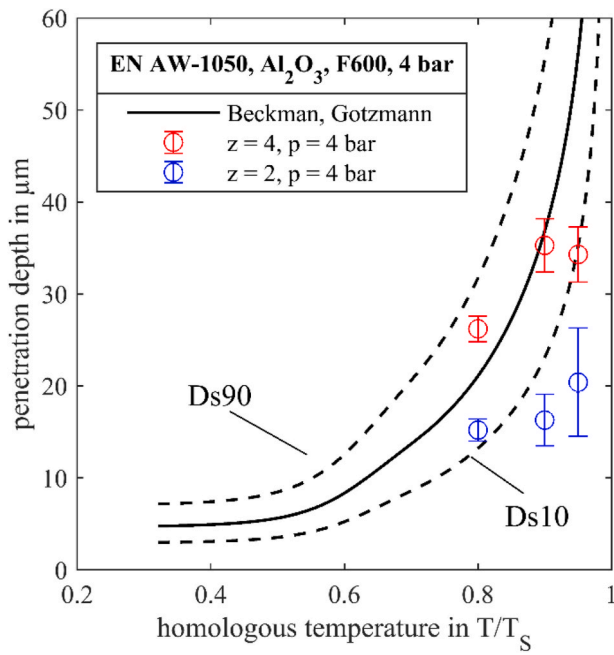


Fig. 13. Comparison of the penetration depth of  $\text{Al}_2\text{O}_3$  particles for EN AW-1050 for an blasting pressure of 4 bar with the model of Beckmann and Gotzmann.

influence of the coverage is more important at an blasting pressure of 4 bar than at 7 bar. In the case of a fourfold coverage at a process temperature of  $T/T_S = 0.9$ , a penetration depth of 35.3  $\mu\text{m}$  can be observed. The results obtained by the micrograph are within the scatter range of the model at a homologous temperature of 0.8  $T/T_S$ . At higher temperatures, the penetration depth is overestimated.

For EN AW-6082, the same relationship between pressure and penetration depth is observed. Here, the penetration depth of the micrographs is within the scatter range of the particle size distribution, as can be seen in [Fig. 14]. At a homologous temperature of 0.95  $T/T_S$ ,

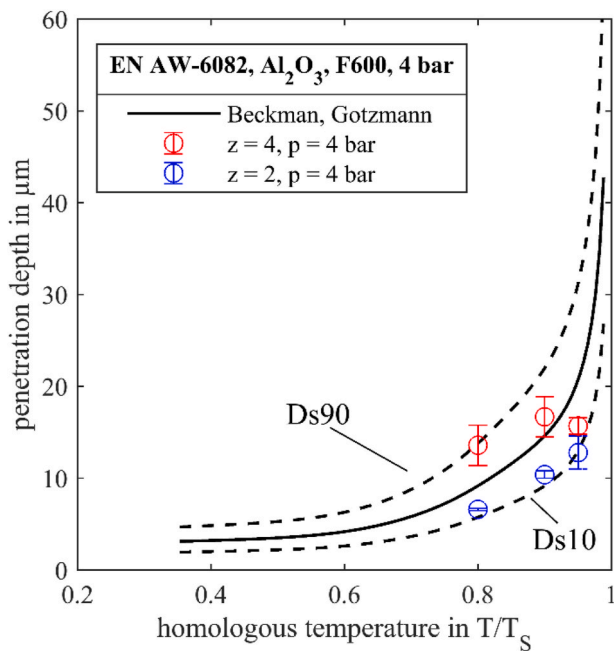


Fig. 14. Comparison of the penetration depth of  $\text{Al}_2\text{O}_3$  particles for EN AW-6082 for an blasting pressure of 4 bar with the model of Beckmann and Gotzmann.

however, both measured values are in the lower range of the model.

4.5. Influence of the blasting particle

The blasting particles influence the penetration depth in the base material by several factors. On the one hand, the kinetic energy of the blasting particles changes due to a different particle size distribution and particle density. On the other hand, the particle shape plays a significant role in the penetration depth. The models address this phenomenon employing shape factors. The penetration depth in composite peening with various blasting particles is shown in [Fig. 15]. The larger particle diameter for the  $\text{Al}_2\text{O}_3$  particles of F320 grain size and the higher density of the WC particles result in an increased penetration depth compared to the smaller  $\text{Al}_2\text{O}_3$  and SiC particles. The model of Beckmann and Gotzmann predicts the latter particles to have a similar penetration depth. At a 0.9  $T/T_S$  homologous temperature, the larger  $\text{Al}_2\text{O}_3$  particles penetrate 24.2  $\mu\text{m}$  into the base material, much less than the model predicts (45.7  $\mu\text{m}$ ). A possible explanation for this may be the particle velocity, which was found to be size-dependent in previous studies in the literature [31, 73]. According to the model of Beckmann and Gotzmann, a lower penetration depth is to be expected for particles with a lower velocity. The penetration depth of WC particles, on the other hand, is underestimated. If the particle distribution is taken as input data for the calculation, however, the penetration depth of the WC particles is within the expected range for both parameter combinations considered.

4.6. Influence of the coverage

Doubling the coverage leads to an increased penetration depth in composite peening for almost every condition considered, as can be seen in [Fig. 10] to [Fig. 14]. Therefore, it can be concluded that an incubation phase, as observed in solid particle erosion of ductile materials, has not yet been terminated. An increase in the penetration depth in the incubation phase was also observed by Ives and Ruff [12] employing micrographs. The incubation phase's duration, or required abrasive mass, depends on many process parameters and can be as long as 20 min in some cases [77]. High particle velocities reduce the particles required and thus the duration, as observed by Neilson and Gilchrist [6].

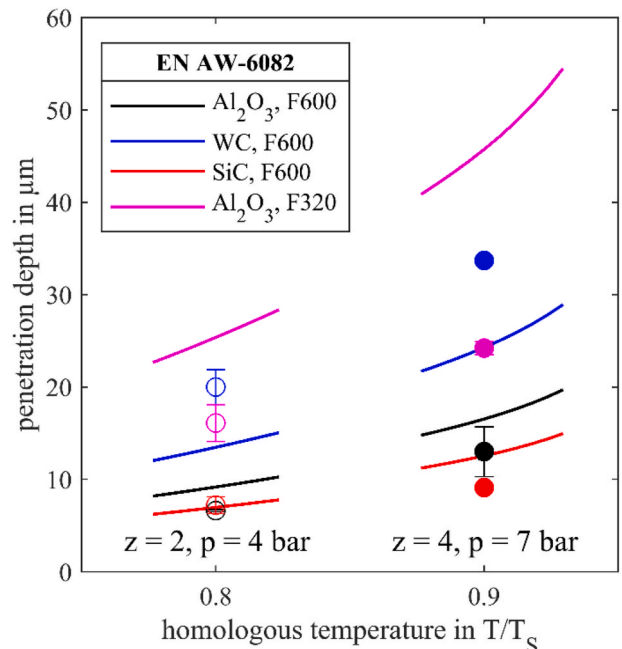


Fig. 15. Comparison of the penetration depth of different blasting particles with the model of Beckmann and Gotzmann for EN AW-6082.

For composite peening, the penetration depth due to multiple processing increases less at a blasting pressure of 7 bar as at a pressure of 4 bar. Although the velocities are similar to  $171 \text{ ms}^{-1}$  to  $193 \text{ ms}^{-1}$ , the mass flow increases by 80% due to the higher pressure. For this reason, the incubation phase should be completed earlier at an blasting pressure of 7 bar. For composite peening, no detailed data are available to determine the incubation phase. However, individual test series with higher coverage do not result in a significant increase in penetration depth. Instead, a buildup of ceramic layers is achieved, which, however, do not exhibit good adhesion properties, as shown by the SEM image in [Fig. 16].

## 5. Discussion

### 5.1. Penetration depth in literature

Particle embedment during solid particle erosion is described often in literature. Many material pairings of particles and base material result in at least particle sticking. In some cases, the penetration depth of such particles is documented by micrographs and can be evaluated. [Table 6]. gives an overview of these data. The penetration depth of the literature data was evaluated directly from the micrographs and represented the maximum detectable penetration depth of the ceramic particles.

In [Fig. 17] the penetration depth of the literature data [12–15,19,46,78] is shown by filled markers. The empty markers depict the corresponding calculated penetration depth according to the model of Beckmann and Gotzmann. Additionally, one parameter set of the composite peening is added (EN AW-1050,  $\text{Al}_2\text{O}_3$ , F600,  $T/T_S = 0.9$ ,  $z = 4$ ,  $p = 7 \text{ bar}$ ). Particle velocities were lower in the literature compared to the composite peening process, ranging from  $20 \text{ ms}^{-1}$  to  $122 \text{ ms}^{-1}$ . In case of smaller particles below  $100 \mu\text{m}$ , particle fragments up to a depth of  $30 \mu\text{m}$  were found in copper [15]. Larger blasting particles resulted in greater penetration depths regardless of the base material. At a particle size of  $600 \mu\text{m}$ , fragments of glass spheres penetrated to nearly  $300 \mu\text{m}$  into the base material [19]. The blasting time is not clearly stated for all investigations. If indicated, a blasting time of at least 10 min was applied.

In contrast to the data from the literature, the blasting particles in this study penetrate deeper than their diameter into the base material during composite peening. The higher particle velocity in combination with the low mechanical properties at high homologous temperatures is most likely to be responsible for this effect. The material properties of the base material for the calculation of Beckmann and Gotzmann model are taken from the CES EduPack database [70] and depicted in [Table 7]. For the literature data, the model estimates the penetration depth of the jet particles to be too low except for one data point.

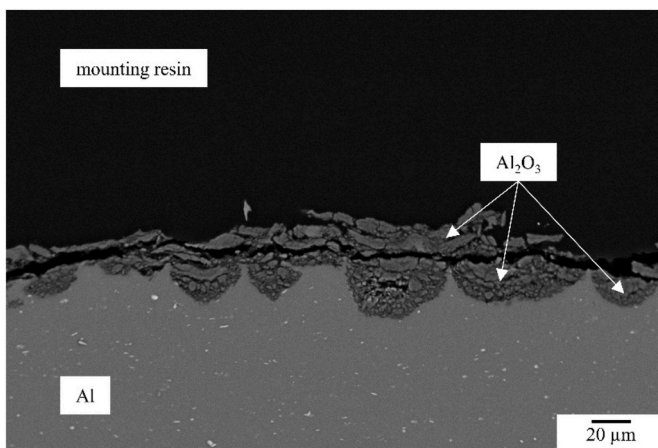


**Fig. 16.** Buildup of a ceramic layer with poor adhesion properties after twelve-fold coverage with  $\text{Al}_2\text{O}_3$  particles for EN AW-1050.

**Table 6**

Penetration depth of ceramic blasting particles in the literature.

Literature	Base material	Blasting particle	Diameter in $\mu\text{m}$	Velocity in $\text{ms}^{-1}$	Penetration depth in $\mu\text{m}$
[14]	Al 1100, 285 °C	SiC	250–300	30	67
[12]	Cu–O	$\text{Al}_2\text{O}_3$	35–65	20	3
[12]	Cu–O	$\text{Al}_2\text{O}_3$	35–65	61	8
[15]	Cu–O	glass	70	122	30
[78]	Fe–O	glass	200	122	42
[13]	Al 1100–O	glass	210	122	67
[19]	Al	glass	600	60	277
[46]	Al 1100–O	SiC	600	61	102

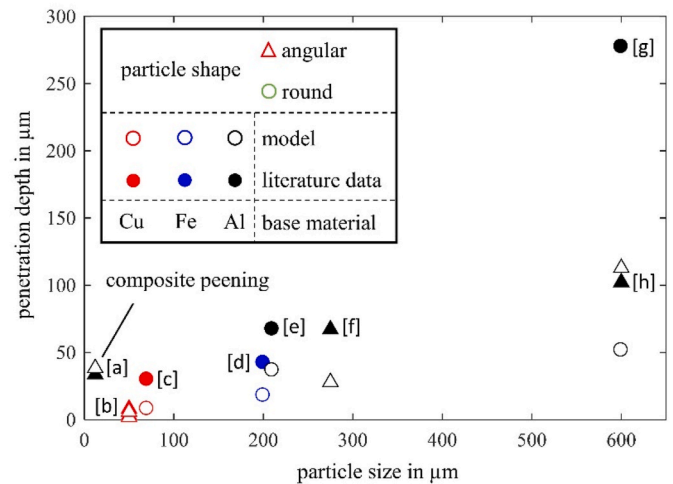


**Fig. 17.** Penetration depth of ceramic particles in solid particle erosion studies (filled markers) and the corresponding calculated penetration depth according to the model of Beckmann and Gotzmann (empty markers). The following assignment applies:

[a] Composite peening: EN AW-1050,  $\text{Al}_2\text{O}_3$ , F600,  $T/T_S = 0.9$ ,  $z = 4$ ,  $p = 7 \text{ bar}$ .  
 [b] Ives and Ruff, Cu, annealed,  $\text{Al}_2\text{O}_3$ ,  $35 \mu\text{m}$ – $65 \mu\text{m}$  [12].  
 [c] Brown and Edington, Cu, annealed, glass spheres,  $70 \mu\text{m}$  [15].  
 [d] Brown et al. Fe, annealed, glass spheres,  $200 \mu\text{m}$  [78].  
 [e] Brown et al. Al, annealed, glass spheres,  $210 \mu\text{m}$  [13].  
 [f] Doyle and Levy, Al,  $285 \text{ °C}$ , SiC,  $250 \mu\text{m}$ – $300 \mu\text{m}$  [14].  
 [g] Cousens and Hutchings, Al, glass spheres,  $600 \mu\text{m}$  [19].  
 [h] Finnie et al. Al, annealed, SiC,  $600 \mu\text{m}$  [46]. (For interpretation of the references to colour in this figure legend, the reader is referred to the Web version of this article.)

**Table 7**

Mechanical properties of the base materials [70].

	Fe, annealed	Cu, annealed	Al, annealed
Young's modulus	208 GPa	125 GPa	70.5 GPa
Hardness	735 MPa	441 MPa	196 MPa

However, the model is of the same order of magnitude for all data and thus can provide a qualitative estimation for the penetration depth.

### 5.2. Application limits of the models

As mentioned above, the models presented describe the penetration depth of a single particle. In the case of composite peening and solid particle erosion, there are multiple impacts of the blasting particles on the same spot. No coverage values are given for solid particle erosion studies in the literature. However, a significantly higher degree of coverage can be assumed in the case of a similar mass flow rate, but

significantly longer operation. This fact may be responsible for the lack of agreement between model and literature values.

Despite the multiple impacts of the particles, the model of Beckmann and Gotzmann reliably describes the penetration depth in composite peening for a large set of process parameters. In [Fig. 18], the models of Ellermaa and Chen and Li are shown additionally. The calculations of Ellermaa are very close to those of Beckmann and Gotzmann since dynamic hardness is calculated as material resistance instead of hardness. For the section considered, the model of Ellermaa describes the penetration depth slightly better than the model of Beckmann and Gotzmann. In the case of composite peening, however, no correction factor for particle size is required. If the correction factor for particle size is included in the equation, the model gives penetration depths ten times smaller. However, at high homologous temperatures, the penetration depth is overestimated by Ellermaa's model, too. The calculations of Chen and Li, on the other hand, predict a smaller penetration depth over the entire temperature range. While at low temperatures, the penetration depth is significantly underestimated, the model of Chen and Li agrees well with the measured values at a homologous temperature of  $0.95 T/T_S$ . One explanation for this may be a change in material behavior. While a pronounced plastic deformation of the base material is still assumed for a Best number  $BN = 10$ , higher velocities or lower material resistance lead to hydrodynamic deformation mechanisms [60]. These mechanisms are successfully modelled in ballistics using cavity expansion models. This consideration is used in the model of Chen and Li. The Best number as a function of process temperature is included in [Fig. 17]. While the Best number at the process temperature of  $0.8 T/T_S$  and a particle velocity of  $193 \text{ ms}^{-1}$  is close to the limit at just under  $BN = 20$ , the Best number gradually increases at high process temperatures due to lower material resistance. For the highest homologous temperature ( $0.95 T/T_S$ ), a value of  $BN = 147$  results for the Best number and consequently a transition from plastic to hydrodynamic deformation mechanisms.

For EN AW-6082, the higher mechanical properties result in a lower Best number, as shown in [Fig. 19]. For a homologous process temperature of  $0.95 T/T_S$ , the Best number of nearly  $BN = 20$  is significantly lower than an case of EN AW-1050. Although the models of Beckmann

and Gotzmann slightly overestimate the penetration depth at this temperature, the cavity expansion model of Chen and Li, on the other hand, predicts a too low penetration depth. This implies that a superposition of both plastic and hydrodynamic mechanisms may be present in the transition region above a Best number of  $BN = 10$ .

For a lower blasting pressure of 4 bar, the lower particle velocity leads to a lower Best number. Here, the plastic behavior is dominant at the highest process temperature with the Best number of  $BN \approx 10$ . Accordingly, the penetration depth estimate based on Chen and Li's cavity expansion model turns out to be too low. In contrast, the two models from solid particle erosion are close to the measured values.

Another challenge is the evaluation of the process temperature itself. At a pressure of 7 bar, the composite peening process cools the surface of the base material down by up to 120 K. As a result, the mechanical properties of the base material increase and, consequently, the maximum penetration depth of the blasting particles decreases. By peening the base material from two directions, it is possible to halve this cooling. Nevertheless, the models may slightly overestimate the penetration depth due to the temperature cooling, especially at high process temperatures. At lower temperatures, the cooling is inevitably smaller due to the more minor temperature difference. Furthermore, the sensitivity of the models to the material resistance decreases due to smaller relative changes.

## 6. Conclusion

During composite peening and solid particle erosion, blasting particles penetrate several micrometers into the base material. The penetration depth of the blasting particles depends on several factors. As the evaluation of the micrographs indicates, the penetration depth increases due to a higher process temperature, a higher coverage and depends on the velocity of the blasting particles. However, a further increase in processing time leads to saturation and thus not to an increase in penetration depth.

The influence of these process parameters on the penetration depth can be qualitatively represented via the described models and thus provide an estimation of the penetration depth in composite peening. In

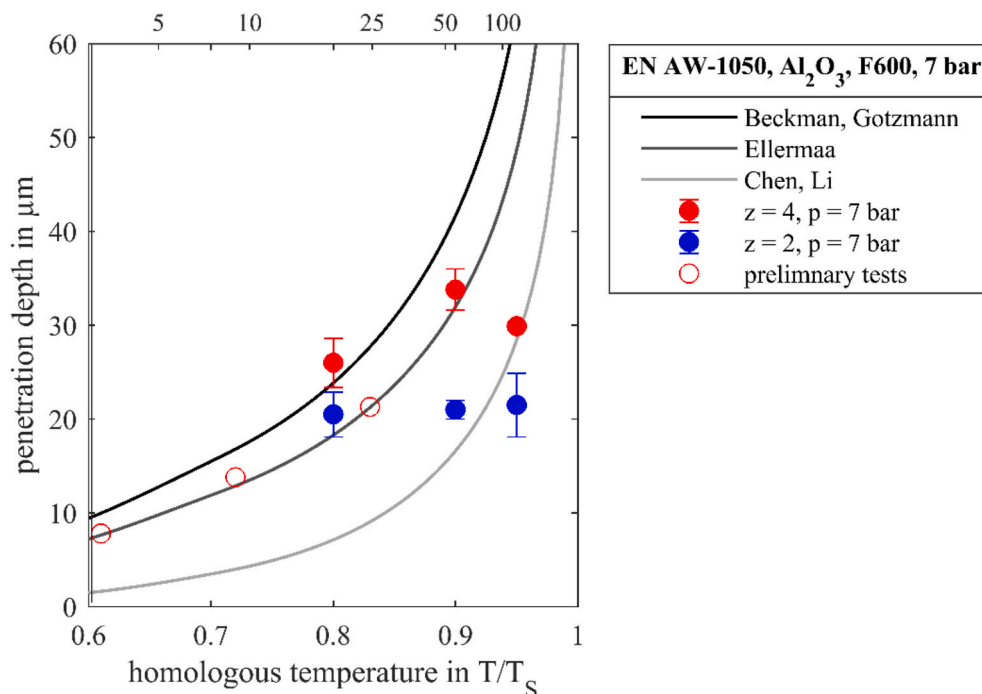
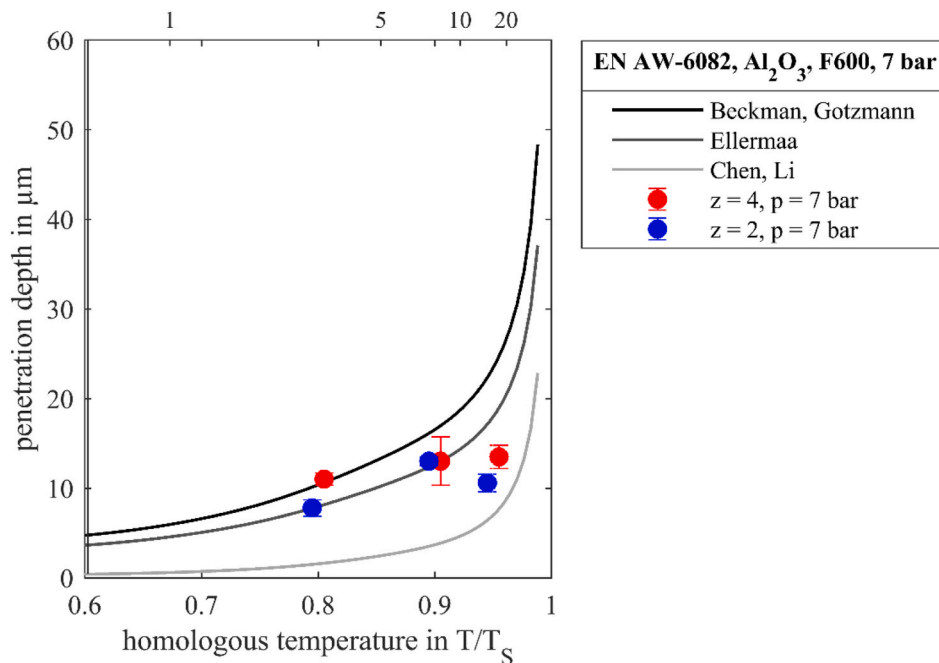


Fig. 18. Comparison of the models from Beckmann and Gotzmann, Ellermaa and Chen and Li for describing the penetration depth in composite peening for EN AW-1050.



**Fig. 19.** Comparison of the models from Beckmann and Gotzmann, Ellermaa and Chen and Li for describing the penetration depth in composite peening for EN AW-6082.

the case of a Best number greater than 10, the models of Beckmann and Gotzmann as well as Ellermaa overestimate the penetration depth in composite peening. This result leads to the conclusion that above the Best number of 10, the elastic-plastic material behavior is increasingly replaced by a hydrodynamic one. The models are also promising for other material systems in solid particle erosion, as the comparison with literature data illustrates. Conversely, it can be concluded for which parameter sets, no penetration is to be expected. This represents an enormous gain if surface contamination is to be avoided, as in shot peening and micro peening treatments.

#### Author statement – PD during CP

Michael Seitz: Methodology, Investigation, Writing - Original Draft.  
Wilfried V. Liebig: Writing – Review & Editing, Supervision.

Kay A. Weidenmann: Writing – Review & Editing, Supervision, Funding acquisition.

#### Declaration of competing interest

The authors declare that they have no known competing financial interests or personal relationships that could have appeared to influence the work reported in this paper.

#### Acknowledgements

The authors would like to thank the German Research Foundation (DFG) for the financial support within the project WE4273/15-1. Furthermore, the authors would kindly like to thank Margarete Offermann and Joachim Binder from KIT, IAM-ESS, for their support and contribution regarding particle size measurements by laser diffraction.

#### References

- [1] C.M. Verpoort, C. Gerdes, Influence of shot peening on material properties and the controlled shot peening of turbine blades, *Metal Behaviour and Surface Engineering*, IITT-International (1989) 11–70.
- [2] K. Shemtov-Yona, D. Rittel, A. Dorogoy, Mechanical assessment of grit blasting surface treatments of dental implants, *J. Mech. Behav. Biomed. Mater.* 39 (2014) 375–390, <https://doi.org/10.1016/j.jmbmm.2014.07.027>.
- [3] M. Ando, H. Kitano, H. Usami, T. Endo, Applicability of fine particle peening on surface modification of aluminum alloy, in: K. Tosha (Ed.), *Proceedings of the 10th International Conference on Shot Peening*, Tokyo, 2008, pp. 223–227.
- [4] Y. Kameyama, J. Komotori, Effect of fine particle peening (PPP) conditions on microstructural characteristics of Ti-6Al-4V alloy, *JMMP 2* (2008) 1338–1347, <https://doi.org/10.1299/jmmp.2.1338>.
- [5] M. Seitz, K.A. Weidenmann, Influence of the process parameters on the penetration depth of the reinforcing phase during composite peening for the production of functionally graded metal matrix composites, *KEM 809* (2019) 73–78. <https://doi.org/10.4028/www.scientific.net/KEM.809.73>.
- [6] J.H. Neilson, A. Gilchrist, Erosion by a stream of solid particles, *Wear* 11 (1968) 111–122, [https://doi.org/10.1016/0043-1648\(68\)90591-7](https://doi.org/10.1016/0043-1648(68)90591-7).
- [7] G.P. Tilly, Erosion caused by airborne particles, *Wear* 14 (1969) 63–79, [https://doi.org/10.1016/0043-1648\(69\)90035-0](https://doi.org/10.1016/0043-1648(69)90035-0).
- [8] A.W. Ruff, S.M. Wiederhorn, *Erosion by Solid Particle Impact*, in: C.M. Preece (Ed.), *Treatise on Materials Science and Technology*, Academic Press, New York, 1979, pp. 69–126.
- [9] P. Shewmon, G. Sundararajan, The erosion of metals, *Annu. Rev. Mater. Sci.* 13 (1983) 301–318, <https://doi.org/10.1146/annurev.ms.13.080183.001505>.
- [10] M. Hassani-Gangaraj, D. Veyssset, K.A. Nelson, C.A. Schuh, Melt-driven erosion in microparticle impact, *Nat. Commun.* 9 (2018) 5077, <https://doi.org/10.1038/s41467-018-07509-y>.
- [11] V. Hadavi, N.H. Arani, M. Papini, Numerical and experimental investigations of particle embedment during the incubation period in the solid particle erosion of ductile materials, *Tribol. Int.* 129 (2019) 38–45, <https://doi.org/10.1016/j.triboint.2018.08.013>.
- [12] L.K. Ives, A.W. Ruff, *Electron microscopy study of erosion damage in copper*, in: W. F. Adler (Ed.), *Erosion: Prevention and Useful Applications*, ASTM International, Philadelphia, 1979, pp. 5–35.
- [13] R. Brown, S. Kosco, E.J. Jun, The effect of particle shape and size on erosion of aluminum alloy 1100 at 90° impact angles, *Wear* 88 (1983) 181–193, [https://doi.org/10.1016/S0043-1648\(83\)80007-6](https://doi.org/10.1016/S0043-1648(83)80007-6).
- [14] P.A. Doyle, A.V. Levy, *The Elevated Temperature Erosion of 1100-O Aluminum by a Gas-Particle Stream*, Materials and Molecular Research Division, Lawrence Berkeley Laboratory, Berkeley, California, 1978.
- [15] R. Brown, J.W. Edington, Erosion of copper single crystals under conditions of 90° impact, *Wear* 69 (1981) 369–382, [https://doi.org/10.1016/0043-1648\(81\)90326-4](https://doi.org/10.1016/0043-1648(81)90326-4).
- [16] S. Söderberg, S. Hogmark, U. Engman, H. Swahn, Erosion classification of materials using a centrifugal erosion tester, *Tribol. Int.* 14 (1981) 333–343, [https://doi.org/10.1016/0301-679X\(81\)90101-8](https://doi.org/10.1016/0301-679X(81)90101-8).
- [17] C.E. Smeltzer, M.E. Gulden, W.A. Compton, Mechanisms of metal removal by impacting dust particles, *J. Basic Eng.* 92 (1970) 639–652, <https://doi.org/10.1115/1.3425091>.
- [18] W.A. Brainard, J. Salik, *Scanning-Electron-Microscope Study of Normal-Impingement Erosion of Ductile Metals*, NASA Technical Paper, Cleveland, Ohio, 1980.
- [19] A.K. Cousins, I.M. Hutchings, A critical study of the erosion of an aluminium alloy by solid spherical particles at normal impingement, *Wear* 88 (1983) 335–348, [https://doi.org/10.1016/0043-1648\(83\)90302-2](https://doi.org/10.1016/0043-1648(83)90302-2).

- [20] J.W. Edington, I.G. Wright, Study of particle erosion damage in Haynes Stellite 6B I: scanning electron microscopy of eroded surfaces, *Wear* 48 (1978) 131–144, [https://doi.org/10.1016/0043-1648\(78\)90143-6](https://doi.org/10.1016/0043-1648(78)90143-6).
- [21] J.W. Edington, I.G. Wright, Study of particle erosion damage in Haynes Stellite 6B II: transmission electron microscopy, *Wear* 48 (1978) 145–155, [https://doi.org/10.1016/0043-1648\(78\)90144-8](https://doi.org/10.1016/0043-1648(78)90144-8).
- [22] V. Hadavi, M. Papini, Numerical modeling of particle embedment during solid particle erosion of ductile materials, *Wear* 342–343 (2015) 310–321, <https://doi.org/10.1016/j.wear.2015.09.008>.
- [23] I. Kleis, H. Uuemõis, Untersuchung des Strahlverschleißmechanismus von Metallen, *Mat.-wiss. u. Werkstofftech.* 5 (1974) 381–389, <https://doi.org/10.1002/mawe.19740050707>.
- [24] J.B. Zu, G.T. Burstein, I.M. Hutchings, A comparative study of the slurry erosion and free-fall particle erosion of aluminium, *Wear* 149 (1991) 73–84, [https://doi.org/10.1016/0043-1648\(91\)90365-2](https://doi.org/10.1016/0043-1648(91)90365-2).
- [25] A.V. Levy, W. Bu-Qian, The effect of test conditions on the erosion-corrosion of alternate low alloy steel tubing alloys, *Wear* 131 (1989) 71–84, [https://doi.org/10.1016/0043-1648\(89\)90246-9](https://doi.org/10.1016/0043-1648(89)90246-9).
- [26] A.V. Levy, M. Yong-Fa, Effect of particle variables on the erosion-corrosion of 9Cr1Mo steel, *Wear* 131 (1989) 53–69, [https://doi.org/10.1016/0043-1648\(89\)90245-7](https://doi.org/10.1016/0043-1648(89)90245-7).
- [27] N. Gat, W. Tabakoff, Effects of temperature on the behavior of metals under erosion by particulate matter, *J. Test. Eval.* 8 (1980) 177–186, <https://doi.org/10.1520/JTE11610J>.
- [28] J. Zhou, S. Bahadur, Erosion-corrosion of Ti-6Al-4V in elevated temperature air environment, *Wear* 186–187 (1995) 332–339, [https://doi.org/10.1016/0043-1648\(95\)07161-X](https://doi.org/10.1016/0043-1648(95)07161-X).
- [29] H. Getu, J.K. Spelt, M. Papini, Cryogenically assisted abrasive jet micromachining of polymers, *J. Micromech. Microeng.* 18 (2008) 115010, <https://doi.org/10.1088/0960-1317/18/11/115010>.
- [30] H. Getu, J.K. Spelt, M. Papini, Reduction of particle embedding in solid particle erosion of polymers, *Wear* 270 (2011) 922–928, <https://doi.org/10.1016/j.wear.2011.02.012>.
- [31] H. Getu, J.K. Spelt, M. Papini, Conditions leading to the embedding of angular and spherical particles during the solid particle erosion of polymers, *Wear* 292–293 (2012) 159–168, <https://doi.org/10.1016/j.wear.2012.05.017>.
- [32] S. Lathabai, M. Ottmüller, I. Fernandez, Solid particle erosion behaviour of thermal sprayed ceramic, metallic and polymer coatings, *Wear* 221 (1998) 93–108, [https://doi.org/10.1016/S0043-1648\(98\)00267-1](https://doi.org/10.1016/S0043-1648(98)00267-1).
- [33] S.M. Walley, J.E. Field, The erosion and deformation of polyethylene by solid-particle impact, *Phil. Trans. Math. Phys. Eng. Sci.* 321 (1987) 277–303, <https://doi.org/10.1098/rsta.1987.0016>.
- [34] J. Zahavi, *Electronmicroscopic Study of Sand Erosion Processes in Metals: No. 041152*, Israel Institute of Metals, Haifa, 1979.
- [35] W. Wu, K.C. Goretta, J.L. Roubort, Erosion of 2014 Al reinforced with SiC or Al<sub>2</sub>O<sub>3</sub> particles, *Mater. Sci. Eng.* 151 (1992) 85–95, [https://doi.org/10.1016/0921-5093\(92\)90185-4](https://doi.org/10.1016/0921-5093(92)90185-4).
- [36] J.L. Roubort, R.O. Scattergood, A. Turner, The erosion of reaction-bonded SiC, *Wear* 59 (1980) 363–375, [https://doi.org/10.1016/0043-1648\(80\)90194-5](https://doi.org/10.1016/0043-1648(80)90194-5).
- [37] M.E. Gulden, Solid-particle erosion of high-technology ceramics (Si<sub>3</sub>N<sub>4</sub>, glass-bonded Al<sub>2</sub>O<sub>3</sub>, and MgF<sub>2</sub>), in: W.F. Adler (Ed.), *Erosion: Prevention and Useful Applications*, ASTM International, Philadelphia, 1979, pp. 101–122.
- [38] J. Salik, D. Buckley, W.A. Brainard, The effect of mechanical surface and heat treatments on the erosion resistance of 6061 aluminum alloy, *Wear* 65 (1981) 351–358, [https://doi.org/10.1016/0043-1648\(81\)90061-2](https://doi.org/10.1016/0043-1648(81)90061-2).
- [39] S. Söderberg, S. Hogmark, H. Swahn, Mechanisms of material removal during erosion of a stainless steel, *ASLE Transactions* 26 (1983) 161–172, <https://doi.org/10.1080/05698198308981490>.
- [40] G.L. Sheldon, I. Finnie, On the ductile behavior of nominally brittle materials during erosive cutting, *J. Eng. for Industry* 88 (1966) 387, <https://doi.org/10.1115/1.3672666>.
- [41] P.G. Shewmon, Particle size threshold in the erosion of metals, *Wear* 68 (1981) 253–258, [https://doi.org/10.1016/0043-1648\(81\)90094-6](https://doi.org/10.1016/0043-1648(81)90094-6).
- [42] G.P. Tilly, A two stage mechanism of ductile erosion, *Wear* 23 (1973) 87–96, [https://doi.org/10.1016/0043-1648\(73\)90044-6](https://doi.org/10.1016/0043-1648(73)90044-6).
- [43] M. Dundar, O. Inal, J. Stringer, The effect of particle size on the erosion of a ductile material at the low particle size limit, *Wear* 233–235 (1999) 727–736, [https://doi.org/10.1016/S0043-1648\(99\)00172-6](https://doi.org/10.1016/S0043-1648(99)00172-6).
- [44] S. Wada, Effects of hardness and fracture toughness of target materials and impact particles on erosion of ceramic materials, *KEM* 71 (1992) 51–74, <https://doi.org/10.4028/www.scientific.net/KEM.71.51>.
- [45] V. Hadavi, B. Michaelsen, M. Papini, Measurements and modeling of instantaneous particle orientation within abrasive air jets and implications for particle embedding, *Wear* 336–337 (2015) 9–20, <https://doi.org/10.1016/j.wear.2015.04.016>.
- [46] I. Finnie, A. Levy, D.H. McFadden, Fundamental mechanisms of the erosive wear of ductile metals by solid particles, in: W.F. Adler (Ed.), *Erosion: Prevention and Useful Applications*, ASTM International, Philadelphia, 1979, pp. 36–58.
- [47] M. Parsi, K. Najmi, F. Najjafard, S. Hassani, B.S. McLauri, S.A. Shirazi, A comprehensive review of solid particle erosion modeling for oil and gas wells and pipelines applications, *J. Nat. Gas Sci. Eng.* 21 (2014) 850–873, <https://doi.org/10.1016/j.jngse.2014.10.001>.
- [48] G. Beckmann, J. Gotzmann, Analytical model of the blast wear intensity of metals based on a general arrangement for abrasive wear, *Wear* 73 (1981) 325–353, [https://doi.org/10.1016/0043-1648\(81\)90299-4](https://doi.org/10.1016/0043-1648(81)90299-4).
- [49] I. Kleis, P. Kulu, *Solid Particle Erosion: Occurrence, Prediction and Control*, Springer-Verlag London Limited, London, 2008.
- [50] R. Ellermaa, Erosion prediction of pure metals and carbon steels, *Wear* 162–164 (1993) 1114–1122, [https://doi.org/10.1016/0043-1648\(93\)90130-E](https://doi.org/10.1016/0043-1648(93)90130-E).
- [51] I.R. Kleis, H.F. Kangur, Resistance of metal surface to indentation by spherical projectile at impact, in: J.E. Field, J.P. Dear (Eds.), *Proceedings 7th International Conference on Erosion by Liquid and Solid Impact*, Cambridge, UK, vol. 48, 1987, pp. 1–7.
- [52] R.F. Bishop, R. Hill, N.F. Mott, The theory of indentation and hardness tests, *Proc. Phys. Soc.* 57 (1945) 147–159, <https://doi.org/10.1088/0959-5309/57/3/301>.
- [53] M.E. Backman, W. Goldsmith, The mechanics of penetration of projectiles into targets, *Int. J. Eng. Sci.* 16 (1978) 1–99, [https://doi.org/10.1016/0020-7225\(78\)90002-2](https://doi.org/10.1016/0020-7225(78)90002-2).
- [54] M.J. Forrestal, K. Okajima, V.K. Luk, Penetration of 6061-t651 aluminum targets with rigid long rods, *J. Appl. Mech.* 55 (1988) 755–760, <https://doi.org/10.1115/1.3173718>.
- [55] M.J. Forrestal, B.S. Altman, J.D. Cargile, S.J. Hanchak, An empirical equation for penetration depth of ogive-nose projectiles into concrete targets, *Int. J. Impact Eng.* 15 (1994) 395–405, [https://doi.org/10.1016/0734-743X\(94\)80024-4](https://doi.org/10.1016/0734-743X(94)80024-4).
- [56] M.J. Forrestal, D.Y. Tzou, E. Askari, D.B. Longcope, Penetration into ductile metal targets with rigid spherical-nose rods, *Int. J. Impact Eng.* 16 (1995) 699–710, [https://doi.org/10.1016/0734-743X\(95\)00005-U](https://doi.org/10.1016/0734-743X(95)00005-U).
- [57] H. Uetz, W. Berndgen (Eds.), *Abrasion und Erosion: Grundlagen, betriebliche Erfahrungen, Verminderung*; 98 Tabellen, Hanser, München, 1986.
- [58] W. Johnson, *Impact Strength of Materials*, Arnold, London, 1972.
- [59] I.M. Hutchings, Mechanisms of the erosion of metals by solid particles, in: W. F. Adler (Ed.), *Erosion: Prevention and Useful Applications*, ASTM International, Philadelphia, 1979, pp. 59–76.
- [60] G. Sundararajan, P.G. Shewmon, The oblique impact of a hard ball against ductile, semi-infinite target materials—experiment and analysis, *Int. J. Impact Eng.* 6 (1987) 3–22, [https://doi.org/10.1016/0734-743X\(87\)90003-0](https://doi.org/10.1016/0734-743X(87)90003-0).
- [61] X.W. Chen, Q.M. Li, Deep penetration of a non-deformable projectile with different geometrical characteristics, *Int. J. Impact Eng.* 27 (2002) 619–637, [https://doi.org/10.1016/S0734-743X\(02\)00005-2](https://doi.org/10.1016/S0734-743X(02)00005-2).
- [62] M.J. Forrestal, A.J. Piekutowski, Penetration experiments with 6061-T6511 aluminum targets and spherical-nose steel projectiles at striking velocities between 0.5 and 3.0 km/s, *Int. J. Impact Eng.* 24 (2000) 57–67, [https://doi.org/10.1016/S0734-743X\(99\)00033-0](https://doi.org/10.1016/S0734-743X(99)00033-0).
- [63] A.J. Piekutowski, M.J. Forrestal, K.L. Poormon, T.L. Warren, Penetration of 6061-T6511 aluminum targets by ogive-nose steel projectiles with striking velocities between 0.5 and 3.0 km/s, *Int. J. Impact Eng.* 23 (1999) 723–734, [https://doi.org/10.1016/S0734-743X\(99\)00117-7](https://doi.org/10.1016/S0734-743X(99)00117-7).
- [64] M.J. Forrestal, N.S. Brar, V.K. Luk, Penetration of strain-hardening targets with rigid spherical-nose rods, *J. Appl. Mech.* 58 (1991) 7–10, <https://doi.org/10.1115/1.2897183>.
- [65] e.V. Deutsches Institut für Normung, *Din EN 573-3: aluminium und Aluminiumlegierungen - chemische Zusammensetzung und Form von Halbzeug - teil 3*, Beuth Verlag GmbH, Berlin 77 (2019), 120.10; 77.150.10.
- [66] J.G. Kaufman (Ed.), *Properties of Aluminum Alloys: Tensile, Creep, and Fatigue Data at High and Low Temperatures*, ASM International, Materials Park, Ohio, 1999.
- [67] J.R. Cahoon, W.H. Broughton, A.R. Kutzak, The determination of yield strength from hardness measurements, *Metall. Trans. A* 2 (1971) 1979, <https://doi.org/10.1007/BF02913433>, 1983.
- [68] D. Tabor, *The Hardness of Metals*, Oxford University Press, Oxford, 1951.
- [69] e.V. Deutsches Institut für Normung, *DIN ISO 8486-2: Schleifkörper aus gebundenem Schleifmittel - Bestimmung und Bezeichnung der Korngrößenverteilung - Teil 2: Mikrokörnungen F230 bis F2000*, vol. 25, Beuth Verlag GmbH, Berlin, 2012, p. 70, 100.
- [70] *Granta Design Limited, Cambridge Engineering Selector 2018*, Granta Design Limited, Cambridge, UK, 2018.
- [71] M. Seitz, A. Reeb, A. Klumpp, K.A. Weidenmann, Composite peening - a novel processing Technology for graded reinforced aluminium matrix composites, *KEM* 742 (2017) 137–144, <https://doi.org/10.4028/www.scientific.net/KEM.742.137>.
- [72] R. Weingärtner, J. Hoffmeister, V. Schulze, Mechanische Oberflächenbearbeitung durch Mikrostrahlen, *Härt.-Tech. Mittl.* 70 (2015) 59–65, <https://doi.org/10.3139/105.110252>.
- [73] S. Kikuchi, Y. Nakamura, K. Nambu, M. Ando, Effect of shot peening using ultra-fine particles on fatigue properties of 5056 aluminum alloy under rotating bending, *Mater. Sci. Eng.* 652 (2016) 279–286, <https://doi.org/10.1016/j.msea.2015.11.076>.
- [74] M. Seitz, L. Karch, K.A. Weidenmann, Preparation methods for electron-scanning and light-microscopic analysis of composite peened aluminium-alumina particle composites, *Pharm. Manag. PM* 57 (2020) 536–544, <https://doi.org/10.3139/147.110635>.
- [75] M. Seitz, M. Dürrschnabel, A. Kauffmann, C. Kurpiers, C. Greiner, K. A. Weidenmann, Characterization of the microstructure after composite peening of aluminium, *Adv. Eng. Mater.* (1–8) (2020) 2000575, <https://doi.org/10.1002/adem.202000575>.
- [76] M. Seitz, K.A. Weidenmann, Mechanical investigations on composite peened aluminium, in: S. Itoh, S. Shukla (Eds.), *Advanced Surface Enhancement*, Springer Singapore, Singapore, 2020, pp. 10–18.
- [77] T. Singh, G. Sundararajan, The erosion behavior of 304 stainless steel at elevated temperatures, *MTA* 21 (1990) 3187–3199, <https://doi.org/10.1007/BF02647314>.
- [78] R. Brown, E.J. Jun, J.W. Edington, Erosion of alpha-Fe by spherical glass particles, *Wear* 70 (1981) 347–363, [https://doi.org/10.1016/0043-1648\(81\)90355-0](https://doi.org/10.1016/0043-1648(81)90355-0).